Journal of Fluids and Structures 118 (2023) 103854

Contents lists available at ScienceDirect

Journal of Fluids and Structures

journal homepage: www.elsevier.com/locate/jfs

Drag reduction on a blunt body by self-adaption of rear flexibly hinged flaps

C. García-Baena [a,b], J.M. Camacho-Sánchez [a,b], M. Lorite-Díez [c,b], C. Gutiérrez-Montes [a,b], J.I. Jiménez-González [a,b,*]

[a] Departamento de Ingeniería Mecánica y Minera, Universidad de Jaén, Campus de las Lagunillas, 23071, Jaén, Spain
[b] Andalusian Institute for Earth System Research, Universidades de Granada, Jaén and Córdoba, Spain
[c] Departamento de Mecánica de Estructuras e Ingeniería Hidráulica, Universidad de Granada, Campus de Fuentenueva, 18071, Jaén, Spain

ARTICLE INFO

Article history:
Received 24 May 2022
Received in revised form 7 February 2023
Accepted 9 February 2023
Available online 26 February 2023

Keywords:
Drag reduction
Bluff body
Passive control
Flexible flap
Self-adaptive flap

ABSTRACT

We study the aerodynamics of a blunt-based body with rear flexibly-hinged rigid flaps, subject to a turbulent flow of Reynolds number $Re = 12000$, under aligned and cross flow conditions with yaw angle $\beta = 0°$ and $\beta = 4°$. To that aim, different values of the equivalent torsional stiffness are considered, to cover the range of reduced velocity $U^* = (0, 3.48]$ in water tank experiments. The effect of the angular deflection of plates on the drag and near wake flow is analyzed, experimentally and numerically. The results show that, in the range of U^* herein considered, the plates undergo an inwards quasi-static, self-adaptive deflection, which is symmetric for yaw angles $\beta = 0°$ and asymmetric for $\beta = 4°$. In particular, the plates feature small mean deformation angles for values of $U^* < 1$, whereas a sharp and monotonic increase of such deflection occurs for $U^* > 1$, i.e. for lower values of the hinge's stiffness, with an asymptotic trend towards the larger values of U^*. A critical value of reduced velocity of $U^* \simeq 0.96$ is obtained as the instability threshold above which plates depart from their initial equilibrium position. The progressive streamlining of the trailing edge translates into significant reductions of the associated mean drag coefficients. Thus, reductions close to 19% with respect to reference static plates configurations are obtained for the most flexible case of $U^* = 3.48$ for both $\beta = 0°$ and $\beta = 4°$. A close inspection of the near wake reveals that the inwards progressive mean displacement of the plates yields a reduction in the recirculation bubble size. A symmetric evolution of the recirculating bubble is observed for $\beta = 0°$, whereas the bubble becomes asymmetric for $\beta = 4°$, with a larger leeward clockwise vortex. In both cases, the drag coefficient is shown to vary linearly with the global aspect ratio of the recirculating bubble. The analysis of the numerical results shows that the reduced extension of the recirculating bubble significantly alters the formation length and intensity of the eddies size and associated pressure. It is observed that despite the local pressure decrease in the vortices shed from the trailing edges, the plates self adaption reduces their size and prevents the eddies from entering the cavity, thus, creating a dead flow region with a consequent pressure increase at the body base.

* Corresponding author at: Departamento de Ingeniería Mecánica y Minera, Universidad de Jaén, Campus de las Lagunillas, 23071, Jaén, Spain.
E-mail address: jignacio@ujaen.es (J.I. Jiménez-González).

https://doi.org/10.1016/j.jfluidstructs.2023.103854

1. Introduction

The reduction of CO_2 and greenhouse gases emission is a fundamental problem in the fight against climate change. In this regard, it is estimated that road transport in heavy-duty vehicles, such as trucks or vans, is responsible for 62% of the global freight transport emissions (International Energy Agency Report, 2018). These kinds of vehicles, which can be considered as bluff-based bodies, are characterized by their poor aerodynamic performance, stemming from the need to maximize the load capacity and optimize unload times. As an example, more than 50% of the total power in heavy duty vehicles in a highway is invested in overcoming the aerodynamic drag (Hucho and Sovran, 1993), of which 25% is attributed to the rear part (Peng et al., 2018; Wood, 2006). The flow around these blunt-based bodies is characterized by a massive flow separation occurring at the edges, which leads to the alternate shedding of vortices and the formation of an intense wake at the rear end. As a consequence, a sizeable recirculation bubble appears close to the base, which is responsible for the generation of a low pressure region. Therefore, these bluff bodies present large values of drag, accompanied by fluctuating side forces, originated from the vortex shedding process, what might result in structural vibrations or stability and maneuverability problems (Hucho and Sovran, 1993).

Numerous studies have been conducted to reduce the aerodynamic forces present on these kinds of bluff bodies. In fact, the use of passive wake control strategies to reduce the aerodynamic drag acting on the flow dynamics at the rear end of vehicles has been extensively analyzed (see e.g. Choi et al., 2014; Szodrai, 2020). Such strategies, which include flaps, vortex generators, splitter plates or rear cavities, among others, constitute appealing solutions, provided their relative simplicity and the absence of external source of energy. A few of these strategies are based on the modification of the size of the recirculation zone in the wake, where an increase in the recirculation bubble length is directly associated to a reduction in the aerodynamic drag (Lorite-Díez et al., 2020a). For example, the use of rigid rear cavities (Khalighi et al., 2001; Verzicco et al., 2002; Sanmiguel-Rojas et al., 2011; Martín-Alcántara et al., 2014; Lorite-Díez et al., 2017, 2018; Bonnavion and Cadot, 2019) has been shown to produce a downstream displacement of the low pressure zone, increasing the pressure at the base of the body and, thus, reducing the aerodynamic drag. In addition, it has been demonstrated that these devices (Choi et al., 2008), regardless of the geometry of the body, are able to weaken the amplitude of the fluctuating forces on the near wake (Martín-Alcántara et al., 2014), modifying the boundary layer detachment and displacing the vortex shedding downstream. However, these devices do not necessarily present an optimal performance for all possible flow conditions, e.g. cross-flow as showed by Lorite-Díez et al. (2020b), what limits their suitability for different real life scenarios and applications. This issue can be partially overcome employing optimization methodologies (Lorite-Díez et al., 2017; Lorite-Díez et al., 2020b) or implementing flexible elements.

The use of flexible structures constitutes an attractive alternative to rigid devices, given their ability to adapt to the flow conditions and modify the rear part of the body to a more aerodynamic shape through passive reconfiguration (Alben et al., 2002; García-Baena et al., 2021a). This process is widely observed in nature, for example, in plants and trees (Harder et al., 2004; Zhang and Nepf, 2020), where the reconfiguration of flexible parts, e.g. leaves, reduce the aerodynamic resistance and the effective area (Vogel, 1989). Nevertheless, the passive reconfiguration of flexible systems has been scarcely investigated in bluff bodies (Abdi et al., 2019). In the study of this fluid–structure interaction problem, the material selection is of great importance (Gosselin et al., 2010). In particular, mechanical properties, such as the flexural rigidity EI, where E is the Young's modulus and I is the moment of inertia with respect to the bending axis, have to be carefully chosen (García-Baena et al., 2021a,b) in order to obtain a valid, viable solution. Flexible plates may undergo elastic instabilities and complex vibrations that hinder the control of the wake and reduction of aerodynamic forces and require thorough and deep analysis. Thus, the consideration of flexible systems characterized by a reduced number of degrees-of-freedom as a first approach is justified by their simpler dynamics, given that they are also able to provide passive reconfiguration and aerodynamic improvement. On that matter, most investigations focus on elastically hinged systems implementing rear plates in cylinders (see e.g. Lu et al., 2016; Wu et al., 2014; Assi et al., 2009). However, there are little studies with hinged plates in blunt-based bodies (most of studies focus on single plate or tandem of hinged plates subject to axial flow, see e.g. Deb et al., 2020). For example, Darbandi and Fouladi (2016) conducted a numerical study on the flow induced vibrations rotatory oscillations of a three-element system. They reported significant variations of the oscillation magnitude for different values of the hinge stiffness, for which a significant decrease in the mean drag and lift fluctuations was also found for low values of the hinge stiffness. Similarly, Mazellier et al. (2012) analyzed the effect of porous rigid movable flaps on the aerodynamics of a square cylinder, reporting reductions of nearly 25% for the drag coefficient. Furthermore, Jiménez-González et al. (2021) studied numerically the flow-induced vibrations of a rear cavity with elastically hinged rigid plates implemented at the base of a blunt body subjected to a laminar flow. The amplitude, frequency and phase response of the system was investigated for different values of the reduced velocity. In general, the flow-induced vibration of the plates has been shown to alter the shedding of vortices and the near wake pressure. However, a proper understanding of these kinds of systems might be of help in the design of improved control flexible strategies.

Under the above conditions, the present paper is focused on the use of a low dynamical order, adaptive control system of two-degrees-of-freedom to reduce the drag of a bluff body and manipulate the wake behind it, with use for both land heavy transport or ocean applications. In particular, the device consists of two flexibly-hinged rigid plates implemented at the rear part of a D-shaped blunt body, tested in turbulent flow conditions, and designed to act as a drag reducer with damped oscillatory response. These mechanically more robust and easier to implement solutions than those which

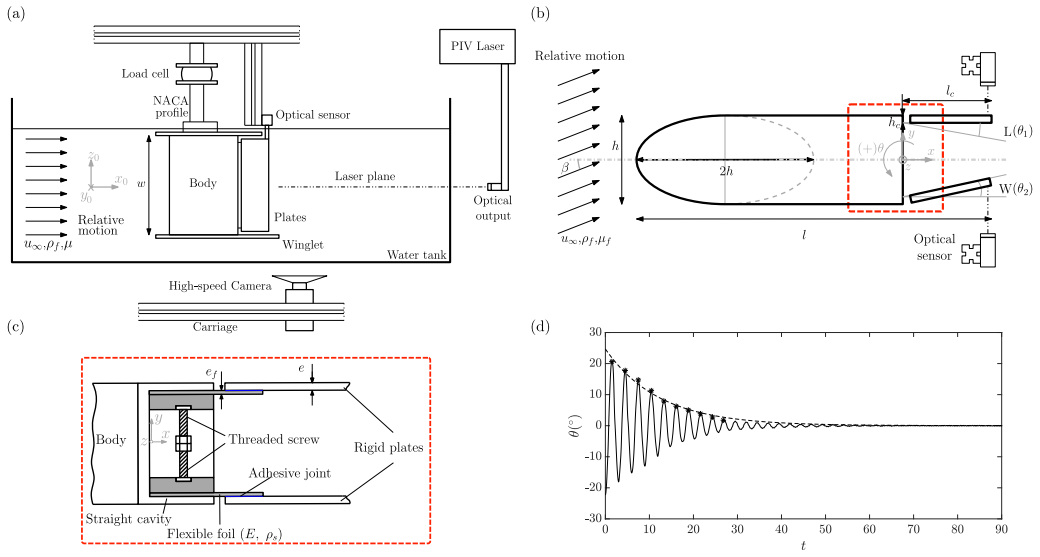

Fig. 1. Sketch of the experimental setup and the body configuration. (a) Side view of the towing tank, the carriage moves from right to left producing u_∞ in the x_o axis direction and sense. (b) Detailed top view of the blunt body of semi-ellipsoidal nose with the yaw angle β formed between the axis of symmetry of the body and the direction of flow. (c) Detailed scheme of the plates tightening system where a threaded screw embeds the flexible plates to a rigid straight cavity at the end of the body. (d) Free decay test in air for $U^* = 2.54$. Global and local coordinates systems, ($Ox_oy_oz_o$) and ($Oxyz$), are also depicted in (a) and (b) respectively.

use flexible structures are able to yield comparable reductions in aerodynamic drag but circumvent the complex solid dynamics of the latter, such elastic transverse instabilities, which renders the former more appealing for engineering applications. In particular, in the present work the effect of different mechanical properties of the system on the drag, plates displacement and near wake flow will be experimentally analyzed, together with results from complementary numerical simulations. The analysis considers both aligned and cross flow conditions, which are usually more demanding in terms of drag coefficient and flow instability, but less commonly evaluated. Therefore, the paper is organized as follows. Section 2 presents the problem description. Next, Section 3 describes technical details of the experimental set-up and the numerical simulations. The experimental results are analyzed in Section 4 while the numerical additional results are reported in Section 5. Finally, the main conclusions of the research and future perspectives are outlined in Section 6.

2. Problem description

We study experimentally the wake behind an extruded blunt base body of height $h = 0.04$ m, length $l = 3.9h$ and width $w = 7.64h$ with a semi-ellipsoidal nose, of major-to-minor axes ratio of 2 (see Fig. 1). The model (García-Baena et al., 2021a) implements a rear cavity formed by two parallel rigid flaps of thickness $e = 0.05h$, length $l_c = 1.375h$ and density, ρ_s. The flaps are mounted employing a torsional joint, built using embedded flexible plates of calibrated thickness e_f and different materials (i.e. brass and steel), as detailed below. Thus, such rotary system of flap and flexible hinge is characterized by an effective torsional stiffness k, damping d, and the mass moment of inertia of the plate J. The values of the equivalent torsional stiffness of the flap-flexible plate system k, will be then varied parametrically by using different materials and thickness for the embedded flexible plates, providing with increasing values of flexural stiffness at the junction EI, where E is the Young's Modulus and $I = we_f^3/12$ is the moment of inertia around the axis of local bending of plates.

When subjected to a uniform fluid stream of constant velocity u_∞, density ρ_f and viscosity μ_f, and with an incident yaw angle β, the body experiences net time-dependent drag force, $\mathrm{f}_x(t)$, and side force $\mathrm{f}_y(t)$, acting respectively on the body-based local x and y axes, belonging to the Cartesian coordinates Oxy, whose origin is placed at the body base, as shown in Fig. 1. Similarly, a global coordinates system Ox_oy_o, referred to the tank, can be also defined, which is coincident with the local system Oxy for $\beta = 0°$. Hence, local forces f_x and f_y can be combined to obtain the drag force in the motion axis along the global axis x_o, $\mathrm{f}_{x,o}$, as

$$\mathrm{f}_{x,o} = \mathrm{f}_x \cos\beta + \mathrm{f}_y \sin\beta \tag{1}$$

(see e.g. Lorite-Díez et al., 2020b). In addition, the rear flaps may undergo rotary oscillations, being $\theta(t)$ the instantaneous angular displacement with respect to the center of rotation at the hinge formed by the flexible plate junction (note that the flaps are mounted with a transverse inward distance of $h_c = 0.075h$ with respect to the lateral edges of the body, what shifts slightly the center of rotation towards an inward transverse location). Since the motion is restricted to angular

rotation, the displacement of leeward (top) and windward (bottom) flaps, ($i = 1$ and 2 respectively, see Fig. 1) can be the modeled using a one degree-of-freedom, angular forced oscillator equation,

$$J\ddot{\theta}_i + d\dot{\theta}_i + k\theta_i = \mathrm{m}_z, \tag{2}$$

where $\dot{\theta}_i$, and $\ddot{\theta}_i$ denote respectively the instantaneous velocity and acceleration of flap $i = 1, 2$, and m_z is the fluid moment with respect to the rotational hinge acting on the plates. Note that the sign criterion for angular displacement is as follows: counter-clockwise rotations are considered positive while clockwise rotations are negative (see Fig. 1b).

A basic dimensional analysis allows the identification of the non-dimensional parameters governing the fluid–structure interaction. Henceforth, all the variables will be non-dimensional, being the characteristic scales of length, velocity, time and pressure used for non-dimensionalization respectively h, u_∞, h/u_∞ and $0.5\rho_f u_\infty^2$. Therefore, the Reynolds number is defined as

$$Re = \frac{\rho_f u_\infty h}{\mu_f}, \tag{3}$$

whose value will be set to 12 000 for the study. The corresponding dominant frequencies of the problem, f, are presented in non-dimensional form, as Strouhal numbers,

$$St = \frac{fh}{u_\infty}, \tag{4}$$

where dominant frequencies can be calculated from the Fourier transform of the corresponding time evolution. Regarding the flaps rotary displacement, the natural frequency of the system's oscillations in vacuum is thus obtained as

$$f_n = \frac{1}{2\pi}\sqrt{\frac{k}{J}}. \tag{5}$$

The dimensionless reduced velocity of the problem can be computed as

$$U^* = \frac{u_\infty}{f_n h} = \frac{1}{St_n}, \tag{6}$$

where St_n is the natural reduced frequency or Strouhal number for $f = f_n$ (Eq. (4)). Thus, the equivalent stiffness of the flap-embedded plate system k, dependent on the flexural stiffness EI of the flexible plate, will change providing different values of the natural frequencies f_n, and consequently the reduced velocity U^*. The natural frequencies are selected to cover the range of reduced velocity $U^* = (0, 3.48]$. Moreover, any oscillation frequency f can be given as a frequency ratio with respect to the natural frequency of plates f_n, as

$$f^* = \frac{f}{f_n}. \tag{7}$$

The flexural stiffness EI of the flexible plates used to build up the elastic torsional junction, can be also given in non-dimensional form by means of the Cauchy number Ca, defined as

$$Ca = \frac{\rho_f u_\infty^2 w l_c^3}{2EI}. \tag{8}$$

Additionally, the dimensionless mass ratio of the system is defined as

$$m^* = \frac{\rho_s}{\rho_f}, \tag{9}$$

whose value will be set to $m^* = 1.33$ for the present study. Besides, the structural damping coefficient of the moving system is computed as $d = 4\xi\pi f_n J$, where ξ is the decay rate that can be characterized experimentally by means of free-decay tests for the flaps in air, which can be also used to estimate the natural frequency (in vacuum) of the system f_n. This is illustrated in Fig. 1(d), where a typical free decay test in air of plates with $U^* = 2.54$ is shown, together with the envelope of the damped oscillations. The different systems of flap and flexible junction are analyzed giving similar rates, being the average value of ξ equal to 0.0225 ± 0.004. Thus, a low mass-damping coefficient is obtained, $m^*\xi = 0.03$.

Finally, the force is made dimensionless as

$$c_i = \frac{\mathrm{f}_i}{0.5\rho_f u_\infty^2 w h}, \tag{10}$$

being c_x the time-dependent drag coefficient in the stream-wise direction, and c_y the time-dependent side force normal to the body width, respectively, measured using the local coordinate system Oxy placed at the base of the body. Similarly, if we consider the global coordinates system $Ox_o y_o$, referred to the tank, and not moving with the body as it is yawed (see Fig. 1), the global drag force coefficient $c_{x,o}$ can be obtained making use of Eq. (1), being naturally $c_{x,o} = c_x$ for $\beta = 0°$. In the following, the body axis drag coefficient will be referred to as drag coefficient, while the motion axis drag coefficient will be referred to as global drag coefficient.

Table 1
Definition of main variables of the fluid–structure interaction problem.

Main parameters	Symbol	Definition	Value (Exp)	Value (Num)
Reynolds number	Re	$\frac{\rho_f u_\infty h}{\mu_f}$	12 000	12 000
Mass ratio	m^*	$\frac{\rho_s}{\rho_f}$	1.33	1.33
Reduced velocity	U^*	$\frac{u_\infty}{f_n h}$	(0, 3.48]	[0.01, 4.27]
Cauchy number	Ca	$\frac{\rho_f u_\infty^2 w l_c^3}{2EI}$	[0.007, 52.272]	[0.001, 305.1]
Yaw angle	β	(degrees)	0°, 4°	0°
Angular plate displacement	θ	(radians)	–	–
Frequency ratio	f^*	$\frac{f}{f_n}$	–	–
(Body axis) Drag coefficient	c_x	$\frac{f_x}{0.5\rho_f u_\infty^2 wh}$	–	–
(Body axis) Side coefficient	c_y	$\frac{f_y}{0.5\rho_f u_\infty^2 wh}$	–	–
(Motion axis) Global drag coefficient	$c_{x,o}$	$c_x \cos\beta + c_y \sin\beta$	–	–
Pressure coefficient	c_p	$\frac{p-p_\infty}{0.5\rho_f u_\infty^2}$	–	–

To complement the experimental results, and validate the permanent regime results from the towing tank, an additional numerical study was performed for selected values of the reduced velocity U^* in the extended range [0.01, 4.27] and nil yaw angle $\beta = 0°$. The study was undertaken by means of turbulent two-dimensional numerical simulations, whose results will serve also to evaluate and test the capability of such simple model to retrieve major features from the fluid-interaction problem. Additionally, this study allowed to retrieve information from the pressure at the wake p while extending the range of torsional stiffness to analyze the limit of quasi-static self-adaption of plates. Thus, for instance, the pressure coefficient is defined as

$$c_p = \frac{p - p_\infty}{0.5\rho_f u_\infty^2}, \tag{11}$$

where p_∞ is the pressure at the incident free-stream. The spatial average of the pressure coefficient at the base allows to obtain the base suction coefficient $c_b = -\langle c_{p,b} \rangle$. A summary of the main variables characterizing both studies is listed in Table 1.

In the following, any time-dependent variable will be denoted using lower case letters, e.g. a, while its temporal averaging will be expressed by means of capital letters, $A = \overline{a}$, unless otherwise stated. Thus, employing the Reynolds notation, $a = A + a'$, with $A' = \sqrt{\overline{(a')^2}}$ being the standard fluctuation. Besides, to evaluate the amplitude of the time-dependent variable a, we will apply the Hilbert transform to obtain the instantaneous amplitude (envelope) $\hat{a}$, whose time-averaged value is expressed as $\hat{A}$.

3. Experimental and numerical details

3.1. Experimental set-up

The experimental study consisted of series of tests performed in a 2 m long towing tank of 0.6 m × 0.6 m test section, where the body is towed from rest until reaching a permanent regime velocity of $u_\infty = 0.3$ m/s, as shown in Fig. 1(a). The acceleration time is set to be short enough (<0.5 s) to ensure a long permanent regime and enough oscillation cycles of flaps for the most demanding case of largest U^*.

The 3D printed body was connected to the towing carriage using a steel shaft holding from a turntable platform, that allowed a precise alignment of the body with respect to the incident stream thus making possible to precisely vary the angle of attack β. As shown in Fig. 1(a), a load cell, rotating with the body, was installed to account for the local forces measurement, f_x and f_y. In addition, two thin acrylic plates were placed at the body ends close to the free surface and ground, to avoid any effect of the free surface waves and ground clearance. A small gap between end plates and flaps was ensured to avoid any interference during vibration. The total blockage ratio of the moving submerged system for the yawed configuration is approximately 7%, which is low enough to avoid important velocity correction, considering that the present study is fundamentally comparative.

Besides, the rear flexible-hinged flaps were installed at the body base using an add-on system that allowed to rigidly hold the metallic foils (brass or steel) with calibrated thickness e, by means of adjustable slits guided by holding screws. Using such holding system, the flexible hinges were located at a small inboard distance of $h_c = 0.075h$ with respect to the rear edges, thus ensuring that the rigid plates remain in line with the body sides. A detailed scheme of the torsional joint built using a tightening screwed system is included in Fig. 1(c). Additionally, a small gap is left between the base and flaps edges, ensuring that the system can freely rotate around the flexible plates' embedment. The gap is small enough to approximate the displacement as that of a one degree-of-freedom hinged-spring oscillator. The dynamic behavior of

Table 2
Main features of embedded flexible plates used in the experimental study.

Foil #	Material	e_f (mm)	E (MPa)	f_n (Hz)	U^*	Ca
1	Brass	0.025	1.1×10^5	2.15	3.48	52.272
2	Steel	0.025	2.1×10^5	2.96	2.54	27.381
3	Brass	0.05	1.1×10^5	5.31	1.41	6.534
4	Steel	0.05	2.1×10^5	6.50	1.15	3.423
5	Brass	0.075	1.1×10^5	9.80	0.77	1.936
6	Brass	0.1	1.1×10^5	11.95	0.63	0.817
7	Brass	0.5	1.1×10^5	–	$\rightarrow 0$	0.007

the system as a one degree-of-freedom oscillator is illustrated with help of Fig. 1(d), where the evolution of the angular oscillations of the plate θ during a free-decay test in air is plotted, alongside the envelope of the damped vibrations. From there, and after application of the Hilbert transform, damping ratio and natural frequency are obtained.

To vary the equivalent stiffness of the hinge, seven different configurations of embedded flexible plates with different materials, brass and steel, and calibrated thickness ($e = 0.025, 0.05, 0.075, 0.1$ and 0.5 mm) were used. Thus, the different junction configurations were initially characterized through free-decay tests in air keeping the body at rest, where the angular displacement of flaps was measured to obtain respectively the corresponding structural damping and natural frequency f_n of the combined flap-flexible plate system, from where the value of reduced velocity U^* is computed, as defined in Eq. (6). These values are listed in Table 2. Note that these represent averaged values for both flaps, since the free-decay tests were applied to the two flaps independently. Finally, the stiffer case #7 is considered as the rigid reference, i.e. $U^* \rightarrow 0$.

3.2. Measurements of displacement of flaps, drag force and flow velocity

The flow-induced displacement of the rear flaps was recorded by means of optical laser sensors (model Leuze ODSL-8/VC66-200-S12), that were towed with the body along the canal, and were installed as displayed in Fig. 1. These sensors measured the linear displacement of the flaps' tips, from which, after application of adequate trigonometric transformation, the instantaneous flaps' angular location θ was provided. The linear resolution provided by the laser translates into an angular accuracy of 0.0005 rad.

Additionally force measurements were performed by means of a load cell (model SRI M3703A) placed below the holding system and the body (see Fig. 1). The load cell did rotate with the body as the yaw angle was modified, so that measurements were obtained in terms of the local reference system Oxy and subsequently composed using Eq. (1) to obtain the global drag along the motion axis x_o. The data acquisition frequency was 1 kHz, and 6 runs were performed for each different hinge configuration to ensure repeatability of results. The accuracy of the load cell was ± 0.001 N, what corresponds to an approximate uncertainty of 0.002 for c_x.

In view of the reported experimental and numerical results in the literature (see e.g. Park et al., 2006; Pastoor et al., 2008) and the previous studies undertaken in the same facility (e.g. Lorite-Díez et al., 2018; García-Baena et al., 2021a) for similar D-shaped bodies, which reported nearly uniform flow variable distributions along the spanwise coordinate at the base and near wake, the employed set-up used herein can be considered to induce a quasi-two dimensional flow in a first approximation, specially with the use of end plates at the body laterals. Thus, near-wake velocity fields in the x, y plane (2D-2C) were obtained by means of time-resolved Particle Image Velocimetry (TR-PIV) at a fixed spanwise location, $z = 0$. The measurements were performed using a 5 W Diode-Pumped Solid State (DPSS) green laser, that illuminated from behind the body, synchronized with a CMOS-sensor, 12 bit, 1 Mpixel High-Speed Camera, located at the bottom of the carriage and towed alongside the body (Fig. 1a). This set-up provided with an approximate Field of View (FoV) of $3h \times 2h$ behind the body, which allowed to properly capture the near wake. The images were recorded with a resolution of 1024×1024 pixels and an acquisition rate of 1000 fps (recording at least 300 images per vortex shedding cycle, and covering between 4 and 6 shedding cycles, depending on the value of U^*). Post-processing of images was performed using the MATLAB® toolbox PIVlab (Thielicke and Stamhuis, 2014). To account for the differences of velocity in the region of interest, three distinct consecutive interrogation windows of respective sizes of 64×64, 32×32 and 16×16 pixels, were used in combination with a 50% overlapping area. As a result, a vector field of 124×62 and a spatial resolution of $0.034h$ was obtained, with the number of spurious vectors obtained being very small and always less than 1% of the total. Thus, given the high temporal resolution of our measurements and the repetitive behavior of the vortex shedding process, very smooth averaged fields were obtained. In addition, the characteristic shedding frequency was also acquired from transverse velocity PIV data and complementary measurements using a one-dimensional, LDV system (model MSE miniLDV™). Further details on these experimental procedures and uncertainty estimation of PIV measurements are provided in García-Baena et al. (2021a).

All the experimental results reported herein have been computed once the permanent conditions were properly checked in our measurements, then, time-averaging is performed for each test. The associated uncertainties and mean values are obtained from those tests performed at each U^* condition.

3.3. Numerical model

The numerical study aims to complement the previous experimental analysis at $\beta = 0°$. To that aim, selected values of the parameters, covering a extended range of reduced velocity $U^* = [0.01, 4.27]$ and the equivalent Cauchy number $Ca = [0.001, 305.1]$ are considered. Note that, as explained below, the numerical hinge is mechanically different from the experimental one, and the value of Ca cannot be computed from any numerical flexural stiffness EI, so that values of Ca are inferred from the experimental correlation $Ca = Ca(U^*)$ and numerical values of reduced velocity U^*, which can be properly established in simulations, after computation of f_n (Eq. (5)).

Therefore, the fluid–structure interaction problem of the flow around the body implementing the flexible hinged plates was studied by means of 2D numerical simulations, assuming that no variation occurs in the spanwise direction. Therefore, the transient, turbulent flow of an incompressible fluid, of density ρ_f and viscosity μ_f equal to those of water, was considered, whereas the flexible junctions of the plates with the rigid body were modeled as a torsional spring of mass moment of inertia J, torsional spring stiffness k, and damping coefficient d. From here, the natural frequency of oscillation of plates was computed as detailed in Eq. (5), to subsequently obtain the reduced velocity U^* (see Eq. (6)).

The computations were conducted using the open source CFD finite-volumes toolbox OpenFoam® (OpenCFD, 2016). To that aim, the solver pimpleDyMFoam, which was used in a previous work (Jiménez-González et al., 2021), was employed, implementing an Unsteady-Reynolds-Average-Navier–Stokes (U-RANS) $k - \omega SST$ model (Menter, 1994; NASA Langley Research Center and Rumsey, 2015). The plates' movement was modeled as a one angular degree-of-freedom rigid body transient motion using the 6-DoF solid-body mesh motion solver that applies SLERP interpolation of movement as function of distance to the object surface and an Arbitrary Lagrangian-Eulerian (ALE) moving mesh technique (Jasak and Tukovic, 2010). Thus, the plate's dynamics was considered as an angular forced oscillator (Eq. (2)), with the center of rotation being the hinge-like junction located at the body rear, as in Jiménez-González et al. (2021) (only a pair of fluid numerical cells are set between the base of the main body and the plate to prevent numerically the flow between the two sides of the plate and to create some space to avoid the physical interference between solid base and moving plates in their oscillation). The experimentally determined values of J and d were used as input parameters, while k was selected and varied to provide with different values of U^* within the range defined in Table 1. Second-order discretization schemes were used both in space and time. The PIMPLE algorithm was used for the pressure–velocity coupling (OpenCFD, 2016), which is suitable to solve transient problems of relatively high Courant numbers. The body motion was solved through an ALE algorithm, that allows to compute the displacement and velocity fields from the moving plates (moving boundaries). The solver deforms the mesh region affected by the plates motion following a Laplace equation, applied to the cell displacement, in such a way that the level of mesh deformation is controlled by means of a diffusivity coefficient in the Laplacian term (Jasak and Tukovic, 2007). Finally, numerical stability was ensured by limiting the time step to obtain a maximum Courant–Friedrichs–Lewy (CFL) number of 0.2 (which yielded maximum dimensionless time steps smaller than $\Delta t \simeq 5 \times 10^{-3}$).

The computational domain reproduces the experimental set-up (Fig. 1), i.e. a blunt base body with rounded nose of height h and length l, implementing two hinged parallel rigid flaps of thickness e, length l_c and density ρ_s, surrounded by a fluid of density ρ_f and viscosity μ_f those of water. The global dimensions of the rectangular domain were selected to assure no influence of the boundaries on the solution, as in Jiménez-González et al. (2021). In particular, the body was placed at the half-height of the domain, of total height $21h$ and at a length of $10h$ downstream from the inlet, and $30h$ upstream from the outlet. Appropriate conditions were imposed at the boundaries, namely, a uniform free stream flow of velocity $(u_\infty, 0, 0)$ and turbulence intensity 0.5% at the inlet, outflow conditions at the outlet, i.e. $\mathbf{n} \cdot \nabla \mathbf{u} = 0$ and $p = 0$, slip condition at the laterals, $\mathbf{n} \cdot \mathbf{u} = 0$ and $\partial p / \partial n = 0$, and no-slip condition at the body. In the previous expressions $\mathbf{n}$ is the outward normal. The computational mesh consisted of a staggered grid, where a stretching was performed near the body and plates, to make sure that $y^+ < 1$, and the wake region is fine enough to resolve the flow with the right spatial resolution (see Fig. 2a,b). The numerical simulations for the different values of U^* were conducted using a converged solution for the base case with rigid plates ($U^* = 0$) as initial condition, obtained after 30 shedding cycles once the permanent regime is reached. Then, the joint stiffness was changed to match the desired U^* and the simulations were run until a sufficiently long period of the corresponding permanent regime is obtained (see Fig. 2c). Finally, the mesh used was selected as a result of a grid convergence study, which was conducted to ensure the grid-size independence of the results. To that end, different simulations were sequentially performed with an increasing number of grid points, starting from a coarse grid with 0.5×10^5 computational cells, see Table 3, for the case of the flow around the body implementing a cavity with the most flexible jointed rotating plates, i.e. $U^* = 4.27$. In comparing results corresponding to different grids, the forces acting on the body were characterized by the time-averaged drag coefficient C_x, and the plates mean angle of rotation Θ. The refinement was continued until the relative difference resulting from consecutive meshes was less than 1.5% for the drag coefficient and less than 2.5% for the mean angle of rotation, see Table 4. Thus, mesh #4 (with 2×10^5 cells) was finally used in our simulations. For further details on the methods and complementary studies, the reader is referred to Jiménez-González et al. (2021).

In the numerical results shown next, the averaged fields are obtained once the flow reaches a permanent regime. Thus, the averaged flow fields are computed using the instantaneous pressure and velocity fields at each time step. For force coefficients and plate deflection, their values are stored at each time step, being their averaged values obtained through post-processing. This temporal average is computed through 20–40 vortex shedding cycles with around 700 (depending on the vortex shedding frequency of the particular case) time steps per cycle.

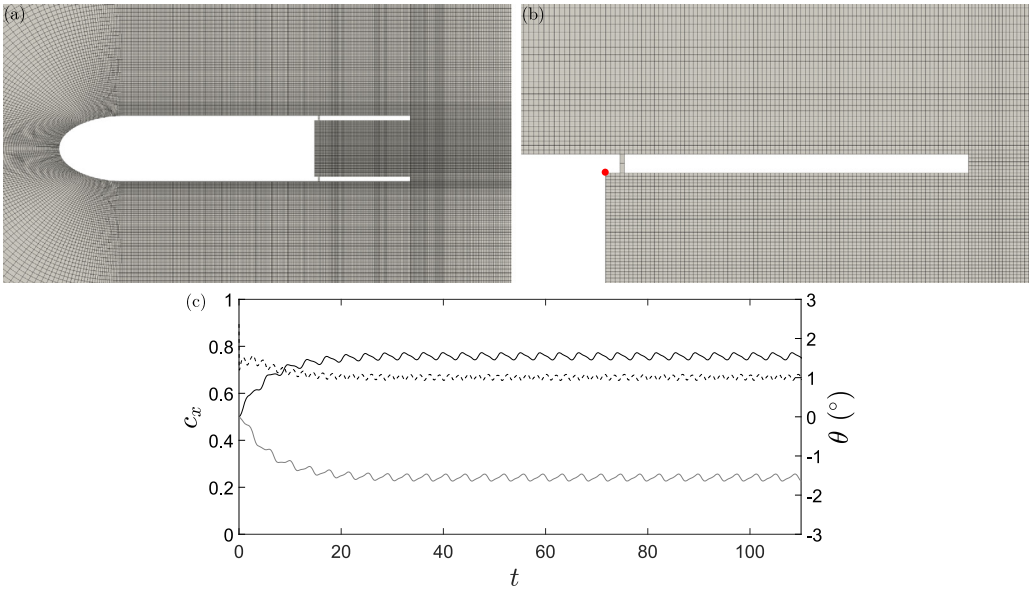

Fig. 2. Grid distribution employed in the numerical simulations: (a) general view and (b) closer view of the grid around the plate. Red dot in (b) represents the hinge location. (c) Temporal evolution of the drag coefficient and plates deflection for $U^* = 1.15$, starting from the converged solution of the base case with rigid plates. Drag coefficient in black dashed line and deflection angles for both plates: θ_2 in dark gray and θ_1 in light gray. Note that, sign criterion for angular displacement is as follows: counter-clockwise rotations are considered positive while clockwise rotations are negative. Given that, both plates will approach each other moving towards inner transverse locations when the lower plate displacement θ_2 is positive and the upper plate displacement is negative θ_1.

Table 3
Meshes used in the grid convergence study: #1 coarse, #2 medium, #3 fine and #4 very fine: n_x and n_y denote respectively total number of nodes in x and y directions, N is the grid size, while Δx and Δy are the characteristic grid resolution in the near wake region.

Mesh	n_x	n_y	N	Δx	Δy
#1	264	194	$\sim 0.5 \cdot 10^5$	$0.019h$	$0.03h$
#2	372	274	$\sim 1 \cdot 10^5$	$0.016h$	$0.022h$
#3	454	334	$\sim 1.5 \cdot 10^5$	$0.014h$	$0.018h$
#4	524	386	$\sim 2 \cdot 10^5$	$0.012h$	$0.014h$

Table 4
Grid convergence study for a blunt-based body with a cavity with the most flexible jointed rotating plates, $U^* = 4.27$ at $Re = 12\,000$, using four different meshes (#1 coarse, #2 intermediate, #3 fine and #4 very fine) based on the time-averaged drag, C_x, characteristic Strouhal number of the periodic vortex shedding at the wake, St_w, and the mean deflection of the plates adaption, Θ. Also shown is the relative error $\epsilon_{j,j+1}$ (%) $= |V(j+1) - V(j)|/V(j) \times 100$, where V is the corresponding variable.

Mesh	C_x	$\epsilon_{j,j+1}$ (%)	St_w	$\epsilon_{j,j+1}$ (%)	Θ	$\epsilon_{j,j+1}$ (%)
#1	0.505	6.10	0.280	4.437	6.685	8.81
#2	0.537	2.26	0.293	–	6.143	4.55
#3	0.550	1.38	0.293	–	5.864	2.13
#4	0.558	–	0.293	–	5.741	–

4. Experimental results

4.1. Analysis of the permanent regime

The analysis of the time-dependent variables is performed within a selected analysis window of the steady regime of the flow. In particular, as described by García-Baena et al. (2021a), the typical time-evolution of drag force corresponding to a body that is initially accelerated from rest and stopped at the end of the run displays two added mass peaks associated respectively to the acceleration and the final deceleration of the towed carriage, and a steady regime in between them. The results of body axis drag coefficient (in the following drag coefficient) c_x and plates' displacement θ for a typical run are illustrated in Fig. 3, for a reduced velocity of $U^* = 1.41$ and $\beta = 0°$. As observed, after a short transient a steady regime is established, characterized by a seemingly sinusoidal oscillation of plates and a nearly constant value of drag.

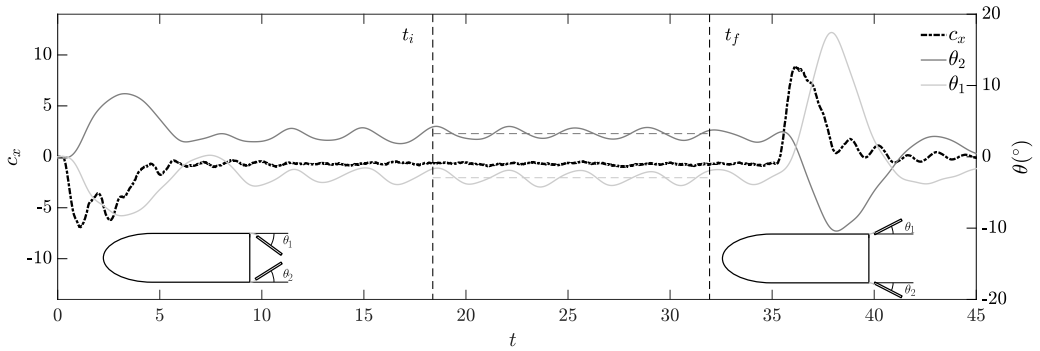

Fig. 3. Experimental measurements of drag force and plates' angle of displacement for $U^* = 1.41$ and $\beta = 0°$. The analysis window of steady regime of drag force (dashed–dotted black line) and displacement angle of plates (light gray solid line - upper plate displacement θ_1; dark gray solid line - lower plate displacement θ_2, see Fig. 1) and corresponding average values Θ (dashed gray lines), lying between limits t_i and t_f defined with vertical lines. Simplified sketches of the displacement of plates during acceleration and deceleration are also included for illustration purposes.

The limits of the analysis window were selected to ensure statistical convergence of the standard deviation of the drag using moving averages of 0.3 s, and to include at minimum of 4 cycles of plates' oscillations. A further discussion on whether the run length is sufficient to provide a steady drag value can be found in García-Baena et al. (2021a) (note that a similar facility is employed in Satheesh and Huera-Huarte, 2019). Finally, at least 6 runs were performed for each value of U^* to ensure repeatability of the results. In addition, some initial tests were run in a water channel facility, available originally at the laboratory (dimensions of test section are 2.5 m $\times$ 0.4 m $\times$ 0.4 m), with a steady body to validate the towing tank results for selected values of U^*. Relative errors for the drag force and amplitude and frequency of plates' oscillations were found to be smaller than 4.1% for all cases (note that such errors may be related to constructive and geometrical differences between both facilities). Additional validation of the permanent regime of the flow was also performed computing the permanent run length and comparing it with other validated permanent values reported in the literature for towing facilities testing bluff bodies (see e.g. previous work from the authors García-Baena et al., 2021a, and references therein).

Fig. 3 illustrates the use of the statistical algorithm defined to find the steady regime window and its limits. Thus, the start time t_i of the window and the end time t_f for the drag force $\mathrm{f}_x(t)$ are shown values of t_i and t_f may be sensitive to increase in the reduced velocity, widening the selected time interval. In the selected window the drag force $\mathrm{f}_x(t)$ is averaged, which allows to calculate the average drag coefficient C_x for all cases analyzed. Similarly, during the analysis window of the permanent regime of drag force, the displacement of plates is analyzed, as shown in Fig. 3. Note that, following the sign criterion given in Section 2, both plates will approach each other moving towards inner transverse locations when the upper (leeward) plate displacement θ_1 is negative and the lower (windward) plate displacement is positive θ_2 (see Fig. 1b). As observed in Fig. 3, the displacement of both plates displays in-phase harmonic oscillations over a mean location, which is shifted with respect to the initial position at rest. This average location of plates is computed as the mean value of the displacement signals, Θ, and shown for illustration purposes using dashed lines in Fig. 3. In view of the sign of both plates' displacement (θ_2 is positive while θ_1 is negative), they move towards inner locations once the flow is set, so that the plates come closer in average, making the trailing edge more aerodynamic. Additionally, the amplitude of oscillations is obtained by means of the Hilbert transform, which identifies envelope of signals, from which the averaged value $\hat{\Theta}$ is computed. In addition, frequency of oscillations may be obtained through spectral analysis by taking the Power Spectral Density of signals. To ensure enough spectral resolution, at least four cycles are captured within the window for all the values of U^*. Finally, note that some simplified sketches of the relative location of plates at different stages of the towed motion have been included for illustration purposes and clarity of interpretation of results during acceleration and deceleration stages, i.e. plates are shown to approach each other during acceleration, and separate during deceleration.

4.2. Drag force

Fig. 4(a) displays the evolution of experimental time-average values of drag coefficient C_x and the global drag coefficient $C_{x,o}$ with the reduced velocity U^*, for yaw angles $\beta = 0°$ and 4°. The associated uncertainty is also included, which is found to be lower than 2.4% in all cases. It is shown that values of C_x ($\beta = 4°$) are higher than those of C_x ($\beta = 0°$), as expected from a presumably more abrupt flow separation at the rear under cross-flow (Lorite-Díez et al., 2020b). In general, regardless of the value of β, as the reduced velocity increases (the stiffness of flexible hinges decreases) for $U^* < 1$, the drag C_x is only slightly reduced, and the trends display similar plateaus. However, for $U^* > 1$ the drag coefficient reduces abruptly, showing a monotonous decrease in both cases. It should be noted that, both curves are nearly parallel for low values of U^*, but they approach at higher values of U^*, indicating that the reduction in drag induced by flexibly hinged plates is more efficient under cross-flow than for aligned conditions. To quantify these drag reductions,

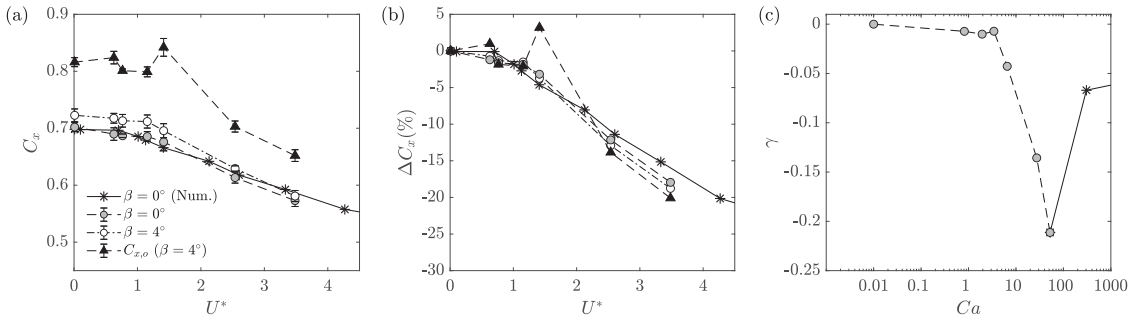

Fig. 4. Evolution with the U^* as a function of the yaw angle β of (a) time average drag coefficient C_x and global drag coefficient $C_{x,o}$ for $\beta = 4°$, where experimental uncertainties are included with error bars, and (b) corresponding relative percentage variation of C_x and $C_{x,o}$ with respect to the reference rigid case, ΔC_x and $\Delta C_{x,o}$. (c) Evolution of the estimate of equivalent Vogel exponent as a function of the Cauchy number Ca for experiments with $\beta = 0°$. Dotted symbols represent experimental values, while numerical results are displayed using asterisks. In (c) solid line represents numerical estimation of γ for the extended range of Ca.

we present in Fig. 4(b) the corresponding relative variations with respect to the reference cases of rigid plates (case #7 in Table 2) for both yaw angle values, i.e. $C_{x,ref}(\beta = 0°) = 0.698$ and $C_{x,ref}(\beta = 4°) = 0.723$. As observed, similar relative reductions are attained, with maximum values being approximately 18% and 19% for $\beta = 0°$ and 4° respectively.

In addition, when the global drag coefficient along the motion axis x_o is considered, similar trends to those obtained at $\beta = 0°$ are observed for $\Delta C_{x,o}(\beta = 4°)$ in Fig. 4(b), with nearly identical maximum reductions with respect to the reference static case (note that $C_x(\beta = 0°) = C_{x,o}(\beta = 0°)$). However, important quantitative differences are observed in values of $C_{x,o}$ on account of the effect of the local side force C_y (see Eq. (1)). Under aligned conditions, the side force is nil due to the symmetry of the configuration, and it does not affect the drag. However, at $\beta = 4°$, the yaw induces transverse pressure gradient between both sides of the body, in such a way that the static case ($U^* \to 0$) features a lateral coefficient of $C_y \simeq 1.35$, while it decreases with increasing U^*, until reaching values close to 1 for $U^* > 2.54$, as the plates readapt to flow. Consequently, as depicted in Fig. 4(a), the composed global drag becomes $C_{x,o} = 0.816$ for $U^* \to 0$, but decreases with U^* until reaching $C_{x,o} = 0.66$ for $U^* = 3.48$. Notwithstanding the foregoing, the global drag presents a local increase for $U^* = 1.41$, which will be shown below to coincide with the peak of fluctuating amplitude of plates, that seems to alter the pressure gradients existing between windward (positive pressure) and leeward sides (negative pressure) at the rear part of the body, and therefore, enhances the side force. In any case, such increase in global drag is soon reverted as U^* increases above such value, providing a maximum relative reduction of $\Delta C_{x,o} \simeq 20\%$, as plotted in Fig. 4(b). Thus, it is evident that the performance of flexibly mounted flaps is preserved in terms of drag reduction, under cross-flow conditions. This represents an advantage over classical rigid rear cavities, whose efficiency as drag reducers is considerably hindered under cross-flow (Lorite-Díez et al., 2020b). This result may open up applicative perspective in applications involving bluff vehicles.

The strong reduction displayed by the mean drag force suggests that deflection of flexibly-hinged flaps is taking place as the reduced velocity increases, whereby plates approach each other progressively. Following a previous work from the same team (García-Baena et al., 2021a), and inspired in reconfiguration of pure flexible elements, the influence of such process on the drag can be quantified by means of the Vogel exponent γ computation. In particular, the classical quadratic velocity-drag law at large Re for rigid bodies $F_x \propto U^2$ is modified to a smaller power law $F_x \propto U^{2+\gamma}$, with γ being the Vogel exponent that takes typically negative values (0 and -1 indicate, respectively, quadratic and linear relationships between velocity and drag). Thus, the value of γ has been traditionally employed in problems concerning flexible plates placed transversely to the flow stream, to evaluate the effective front area reduction and the streamlining of the body for different shearing flows. However, as highlighted by García-Baena et al. (2021a), for the current configuration, the value of γ may be used to evaluate the effect of the rear reconfiguration on the recirculation bubble size. To that aim, the Vogel exponent is computed using the following expression

$$\gamma = 2\frac{\partial \ln \Re}{\partial \ln Ca}, \tag{12}$$

where $\Re = C_x/C_{x,ref}$ is the reconfiguration number and Ca is the Cauchy number given for each flexible plates' hinge in Table 2. The evolution of the experimental Vogel exponent with Ca is depicted in Fig. 4(c) at aligned flow conditions $\beta = 0°$. In particular, it can be observed that $\gamma \simeq 0$ for low Cauchy number, but displays negative values for $Ca > 3.423$ ($U^* > 1.154$), from where the quadratic law $F_x \propto U_\infty^2$ no longer holds. The exponent displays an experimental minimum value of -0.21 at $Ca = 52.272$, which is the most flexible case investigated in experiments. As it will be discussed below, numerical simulations allow a first approximation on the extrapolation of the Vogel exponent computation towards higher values of Ca (see solid line in Fig. 4c). This estimation shows an increase of γ to reach -0.06 at the maximum Ca investigated numerically, indicating a limit on the potential decrease of the drag force with the increase of flexibility. This trend resembles that obtained for rear flexible foils by García-Baena et al. (2021a) and suggest a similar self-adaptive process in spite of the mechanical differences between adaptive flaps.

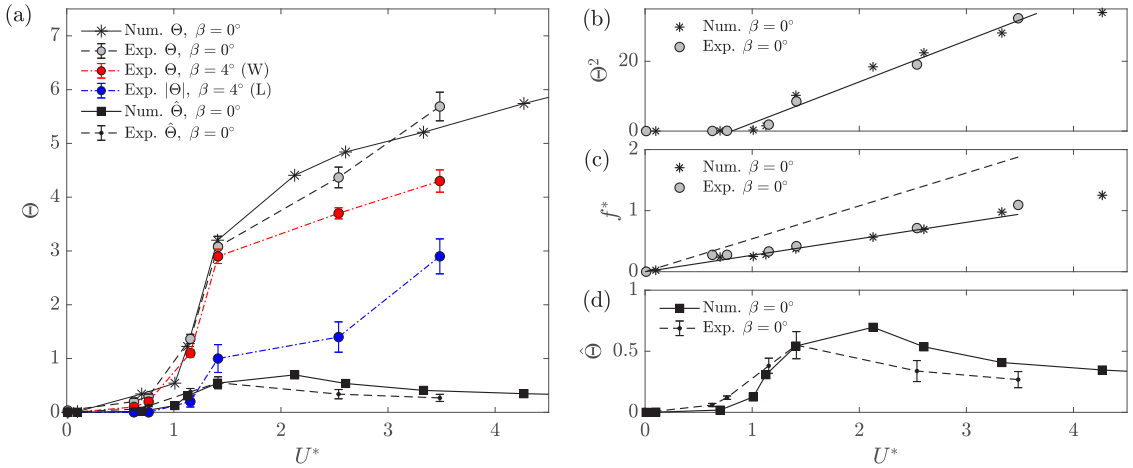

Fig. 5. Evolution with the reduced velocity U^* of (a) mean angular displacement (inwards) of plates Θ and mean amplitude of angular oscillations of plates $\hat{\Theta}$, where experimental uncertainties are included as error bars; (b) square of the time-average angular position Θ^2; (c) frequency ratio $f^* = f_p/f_n$ of plates oscillations; and (d) detail of the mean amplitude of angular oscillations of plates $\hat{\Theta}$, for $\beta = 0$, as shown in (a). In order to represent experimental results in: gray ($\beta = 0°$), red ($\beta = 4°$, windward plate) and blue ($\beta = 4°$, leeward plate) circles are used for Θ while points (with dashed lines) are used for $\hat{\Theta}$. Numerical results ($\beta = 0°$) are displayed using asterisks and solid lines. Solid line in (b) represents the linear fit $\Theta^2 = C_f \cdot \left(U^* - U^*_{cr}\right)$, while the solid and dashed lines in (c) represent respectively the Strouhal law vs U^*, given by the reference rigid cavity body $f^* = St^r_w \cdot U^*$, and its harmonic $f^* = 2\ St^r_w \cdot U^*$, with $St^r_w = 0.29$. (For interpretation of the references to colour in this figure legend, the reader is referred to the web version of this article.)

4.3. Plates displacement

Laser measurements have been used to determine the mean angular displacement (inwards) of both flaps and to characterize their corresponding average position Θ and amplitude of oscillations $\hat{\Theta}$ within the analysis window for the permanent regime. As discussed earlier with help of Fig. 3, both plates oscillate in phase around mean transverse positions, which are shifted transversely inwards as the value of U^* grows. As a result, the plates undergo symmetric time-average angular displacements, and anti-symmetric (in-phase) instantaneous oscillations. Fig. 5(a) displays experimental mean results of both plates for Θ and $\hat{\Theta}$, the latter also shown in Fig. 5(d) for the sake of clarity. The uncertainty corresponding to the measurements of Θ and $\hat{\Theta}$ is also included. As observed, the mean angle Θ shows very low values for $U^* < 1$, meaning that there is little adaption of plates for the stiffer cases of the study. However, for $U^* \geq 1$ there is a sharp increase of the mean angular displacement, that attains a maximum value of 5.7° for the largest U^* investigated. Thus, the trailing cavity defined by flaps becomes progressively more aerodynamic as the stiffness of hinges is reduced, that translates into corresponding reductions of the mean drag coefficient, as illustrated earlier with help of Fig. 4(a). Finally, the mean deflection seems to reach an asymptotic trend at large U^* (noticeable if numerical results are considered, see asterisks in Fig. 5), what may define a practical limit on the self-adaption of plates, and associated drag reduction. This observation is consistent with the increase of the Vogel exponent depicted in Fig. 4(c).

The abrupt increase of the mean angular displacement of plates suggest the occurrence of a bifurcation related to the existence of a critical reduced velocity, i.e. critical effective hinge stiffness, above which plates deflect from their initial equilibrium position. A quantification of such an instability threshold can be obtained, e.g. by using the classical normal form of a pitchfork bifurcation, which is typically used in dynamical systems to predict the departure of unstable dynamics from equilibrium close to the bifurcation (see e.g. Jiménez-González, 2013). To that aim, the square of the mean angular displacement is displayed in Fig. 5(b), where it can be observed that Θ^2 features a linear trend with U^*. Hence, the linear fit $\Theta^2 = C_f \cdot \left(U^* - U^*_{cr}\right)$ can be applied to data (solid line in Fig. 5b), with C_f being a fitting constant and U^*_{cr} the critical threshold of instability. The linear extrapolation of Θ^2 to zero gives a value of $U^*_{cr} \simeq 0.96$.

Additionally, the mean amplitude of flaps oscillations $\hat{\Theta}$ is depicted in Fig. 5(a,d). As observed, the flow-induced oscillations of flaps are of moderate amplitude within the whole range of U^* investigated. In particular, the dynamic response of flaps seems to be similar to the classical three branches (with different amplitudes) response in canonical VIV problems, i.e. initial ($U^* < 1$), upper ($1 \geq U^* \leq 2.5$) and lower ($U^* > 2.5$), being the maximum value of $\hat{\Theta} \simeq 0.7°$, reached at $U^* = 1.41$ within the upper branch. However, this distinction must be considered carefully here due to scarcity of data. The frequency response of flaps is analyzed with help of Fig. 5(c), where the ratio $f^* = f_p/f_n$ is depicted (the characteristic frequency of plates oscillation f_p is obtained by taking the Power Spectral Density Transform of instantaneous angular displacement). Additionally, the Strouhal linear law given by the vortex shedding behind the rigid case, i.e. $f^* = St^r_w\, U^* = 0.29\, U^*$ has been included for comparison. The oscillations frequency of plates is seen to follow in general the Strouhal law given by the rigid cavity (St_r), indicating that the wake dynamics mostly governs the frequency

response of the plate. Interestingly, the values of f^* are above the linear law around $U^* = 1$, defining a sort of plateau, where the upper branch of amplitude response rises. This might be an indication of plates responding close to their natural frequency in water. Note that no valid free-decay tests are available for plates in water, as the motion is quickly damped; nevertheless, a simplified theoretical estimation of the natural frequency in water as $f_{n,w} = (1/2\pi)\sqrt{(k/(J + J_w))}$, where J_w is the polar moment of inertia of the displaced volume of water, provides values of $f_{n,w} \leq f_n/3$ (this approximation does not consider any added mass coefficient and therefore, its use for a deeper analysis of results has been discarded). Besides, the value of f^* for plates oscillations lies also above the linear law of $St_w^r\ U^*$ at large values of U^*. This was also reported by García-Baena et al. (2021a) for flexible foils, where it is discussed that the shedding process accelerates as the distance between rear edges of plates decreases resulting from the progressive reconfiguration with increasing U^*.

Once the response of plates has been analyzed, it can be concluded that the dynamic response of flaps within the range of U^* considered herein is very weak (notice that the amplitude of oscillations $\hat{\Theta}$ represents at most 15% of the mean angular displacement Θ at $U^* = 1.413$ and only a 4% for $U^* = 3.48$), and therefore, the self-adaption can be treated as quasi-static in a first approximation. This may simplify the adaptation of this type of strategy as drag reducer in more complex applications involving, for instance, bluff vehicles.

Considering now the results on the deflection of plates under cross-flow, Fig. 5(a) depicts the evolution of time-averaged displacement Θ for both the windward and leeward plates. As observed, the plates' displacement remains nearly zero for $U^* \leq 1$ and grows abruptly around $U^* = 1$, which has been approximately identified as the threshold of instability for the plates' departure from equilibrium. It is seen that the maximum mean deflections are approximately 4.2° and 2.9° for the windward and leeward plates respectively. Note that such values represent the relative displacement with respect to the initial positions of equilibrium (which are already yawed 4°). Thus, if the trends are analyzed closer, it can be observed that the windward plate features an asymptotic evolution that tends to reach the limit of 4.2° at high values of U^*. Considering that this value is a relative displacement, such result is an indication of the plate's alignment with the flow, compensating the initial yaw angle of $\beta = 4°$. Besides, the leeward plate displays an increasingly growing trend at large U^*. Thus, although the maximum value of the corresponding Θ is 2.9° at $U^* = 3.48$, this trend suggests a larger adaption of plates to flow outside the range of reduced velocity studied here (note also that the equilibrium angular position of the leeward plate for the rigid case under cross-flow is already pointing inwards in the transverse direction to the flow, so that the deflection of the flexible plate may be viewed as an extra reorientation with respect to its initial *tilted* position, what would lead to an effective value of nearly 7°). In any case, the alignment of the windward plate with the flow and the extra increase in Θ for the leeward plate, are seemingly associated with the intense relative reduction of the drag coefficient at large U^* displayed in Fig. 4 (a) for $\beta = 4°$. Finally, it is interesting to note that the side force and, consequently, the global drag seem to be particularly sensitive under cross-flow conditions to the amplified vibration response of the plates reported for $U^* = 1.41$ (Fig. 5a), for its value is clearly enhanced for such configuration of plates (Fig. 4a).

4.4. Near wake visualizations

The modifications of the near wake topology induced by the quasi-static deflection have been evaluated with the help of PIV measurements, performed for selected values of the reduced velocity. First, the effect of the mean plates displacement on the recirculating length is discussed with the help of the time-averaged contours of the axial velocity, $U_x(x, y)$, and the corresponding streamlines, depicted in Fig. 6, for $U^* = 0$, 1.15 and 3.48 and aligned conditions, $\beta = 0°$. It is observed that the progressive mean displacement of plates reduces the size of the recirculating bubble. The deflection induces the flow to leave the rear edges with a higher momentum towards the axis in the y coordinate, resulting into a decrease of the transverse height or bluffness and the shortening of the recirculating bubble with increasing U^*. The modification of the structure of the near wake also reduces the backflow velocity, $U_x < 0$.

On the other hand, the effect of the plates' self-adaption under cross-flow on the near wake is shown in Fig. 7, with help of the corresponding time-averaged contours of axial velocity and flow streamlines for $\beta = 4°$ and the same selected values of U^* used in the previous figure. As observed, the body misalignment induces the deflection of the recirculation bubble which becomes asymmetric. In particular, the leeward clockwise vortex becomes bigger and is located closer to the body base than the windward counter-clockwise vortex. When compared to the aligned case of $\beta = 0°$, the cross-flow tends to enlarge the recirculation bubble which extends over a wider region in the near wake, what may translate into a lower general pressure at the wake, and consequently a larger drag. Besides, the size of the bubble and respective cores of recirculation reduces progressively as U^* grows. This process is induced by the gradual deflection of flaps as the stiffness of plates is decreased. Additionally, the unequal mean deflection of both plates induces an increasing global deflection of the streamlines at the rear stagnation point of the bubble (see Fig. 7c).

To quantify the reorientation of flaps as U^* grows, we compute the mean values of the recirculating bubble bluffness, H_r, and length, L_r, from the PIV measurements. The value of H_r is defined as the gap between the external corners of plates rear edges (it can be also easily derived with help of the displacement measurements presented in Fig. 5), while the length L_r is characterized as the maximum downstream location from the body base ($x = 0$) where $U_x \leq 0$ (thus defined, the value of L_r implicitly includes the cavity length). Note that H_r and L_r are given with respect to the rotated local coordinate system Oxy for $\beta = 4°$. The trends with the reduced velocity U^* of H_r and L_r are respectively depicted in Fig. 8(a) and (b). As observed, the variation of H_r with U^* is very similar to that of C_x shown in Fig. 4, especially for $\beta = 0°$,

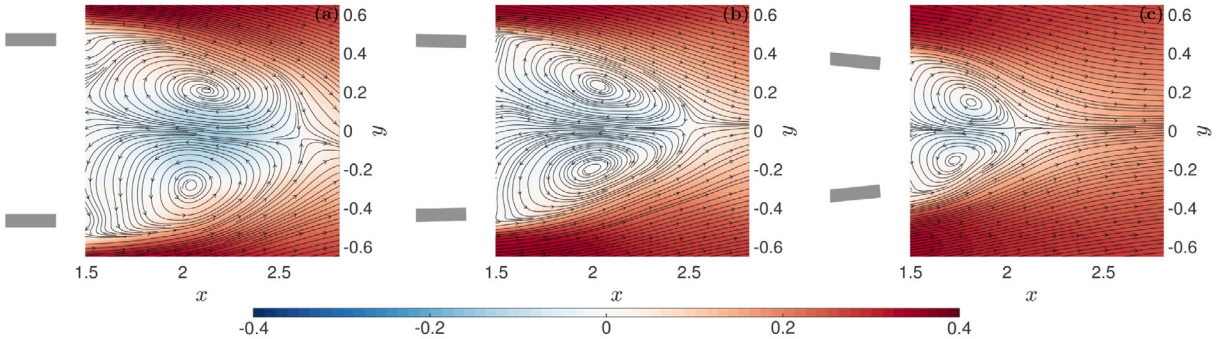

Fig. 6. Time-averaged contours of axial velocity $U_x(x, y)$ and corresponding streamlines for $\beta = 0°$ and (a) $U^* = 0$, (b) $U^* = 1.154$, (c) $U^* = 3.48$. An estimation of flaps location and orientation has been included for illustration purposes.

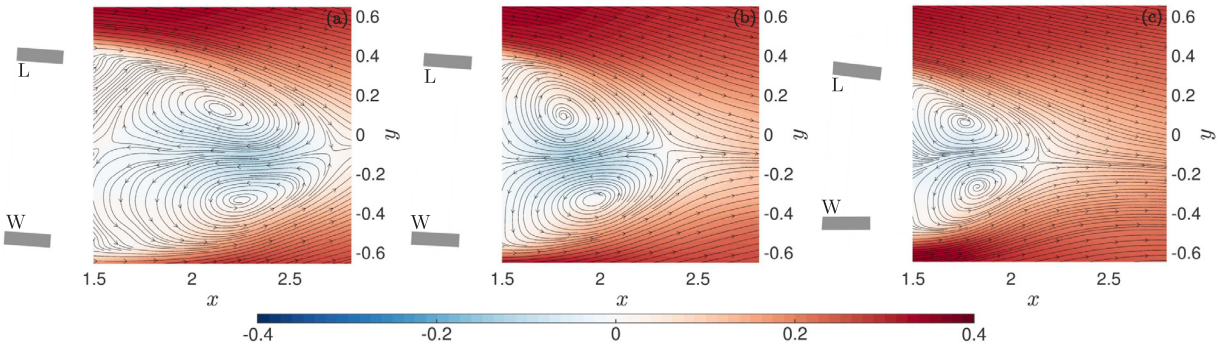

Fig. 7. Time-averaged contours of axial velocity $U_x(x_o, y_o)$ and corresponding streamlines for $\beta = 4°$ and (a) $U^* = 0$, (b) $U^* = 1.15$, (c) $U^* = 3.48$. An estimation of flaps location and orientation has been included for illustration purposes.

whose initial plates' displacement is stronger. In particular, due to its dependence on the evolution of the time-averaged angular deformation of plates (Fig. 5a), very small changes of H_r take place initially with increasing U^* for the stiffer cases, while a sudden decrease occurs for $U^* > 1$. Note that the minimum values of H_r at $U^* = 3.48$ for $\beta = 0°$ and $\beta = 4°$ are respectively $H_r = 0.73$ and 0.80. It should be noted that the trends of H_r for both values of β diverge initially as the adaption of plates is slightly stronger at low values of U^* for $\beta = 0°$ (see Fig. 5a), but become nearly parallel for larger values of U^* when the leeward plate adapts to flow for $\beta = 4°$. In this regard, as expected for a bluffer body with higher drag, the trend of H_r in cross-flow lies above that corresponding to aligned flow conditions. On the other hand, the recirculating length L_r undergoes a similar decrease with increasing U^* for both values of yaw angle, featuring a sharp change around $U^* = 1$, where the mean deflection of plates has been shown to depart abruptly (see Fig. 5b). As we compare rear flaps with the same length, where the separation point is fixed for all the cases, we can also compute the recirculation length relative to the flaps' tip, $L_r - l_c$. The evolution of this distance is depicted in Fig. 8(i).

Following the discussion introduced by García-Baena et al. (2021a) for the reconfiguration of flexible rear foils, the impact of the recirculating bubble bluffness on the drag coefficient can be estimated from H_r. In particular, it was discussed therein that the dependence between both magnitudes can be established by means of an affine direct relationship, that allows to quantify the connection between near wake and flow separation and hidrodynamic improvement provided by the trailing edge streamlining. To evaluate whether the same dependence applies here when flexibly-hinged rigid flaps are used instead of flexible foils, we depict in Fig. 8(c) the mean drag coefficient C_x versus H_r (there, the results for $\beta = 4°$ are given referred to local coordinate axis). The results of $\beta = 0°$ and 4° seemingly collapse on a single trend. From here, it is shown that the mean drag coefficient C_x fairly varies linearly with the near wake bluffness H_r, following the equation

$$C_x = C_{x,ref} + \alpha(H_r - H_{r,ref}), \tag{13}$$

where the values of $C_{x,ref} = 0.72$ and $H_{r,ref} = 1$ have been taken from the rigid reference case for $\beta = 4°$ (largest drag), and α is that maximizing the R-squared fitting coefficient. These results confirm that the reconfiguration process of flexible foils and flexibly-hinged rigid plates are similar in terms of the direct relationship between recirculating bubble size and drag, with the bubble bluffness becoming smaller as U^* (or Ca) increases.

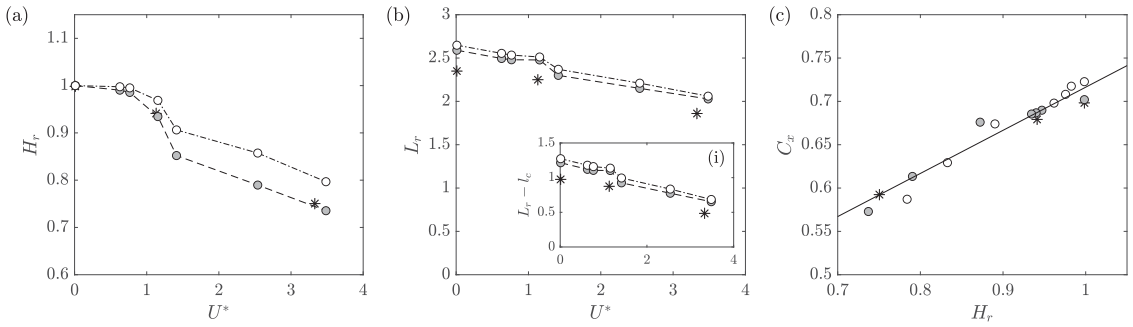

Fig. 8. Main time-averaged magnitudes of recirculating bubble and drag coefficient for $\beta = 0°$ (gray circles) and 4° (white circles): (a) recirculating bubble bluffness H_r and (b) recirculating lengths L_r versus the reduced velocity U^*. (c) Mean drag coefficient versus the bluffness H_r. Numerical results for selected values of U^* are displayed using asterisks, while the solid line in (c) represent the linear fit of Eq. (13). (i) Recirculating lengths, defined from flaps' tip, $(L_r - l_c)$ evolution with U^*.

Another generally accepted result concerning wakes behind blunt-based bodies is that variations of drag coefficient are proportional to variations of the base suction, defined as the negative base pressure coefficient, i.e. $\Delta C_x \propto \Delta(C_b)$. Thus, the relation (13) allows a first estimation of the base pressure recovery induced by reconfiguration of plates. To validate such hypothesis, we next present the numerical results on drag, plates' deflection and wake pressure.

5. Numerical results

As highlighted in Section 2, two-dimensional turbulent numerical simulations are performed to complement the experimental study for $\beta = 0°$ and the extended range of reduced velocity $U^* = [0.01, 4.27]$. First, it will be analyzed whether a simple, unsteady RANS approach is capable of retrieving major variables of the simplified fluid–structure interaction experimental problem. After such a validation of results, the study will help to understand effect of plates' self-adaption on the wake pressure and limits of such process at larger values of reduced velocity.

5.1. Validation of numerical results and limit of plates adaption

We first evaluate the capability of two-dimensional simulations to retrieve major results from experiments. The comparison between numerical and experimental results is done with the help of Figs. 4, 5 and 8. These figures depict numerical results for: the time-averaged drag coefficient C_x and corresponding relative reduction with respect to the reference case of rigid static plates, ΔC_x (Fig. 4); mean deflection of plates Θ, amplitude of oscillations $\hat{\Theta}$ and corresponding frequency ratio f^* (Fig. 5); and size of the recirculating bubble, H_r and L_r (Fig. 8). As observed in these figures, experimental and numerical results describe nearly identical qualitative evaluations with the reduced velocity. Besides, depending on the variable, the quantitative comparison between results shows errors of different magnitude. For instance, values of drag C_x at coincident reduced velocity of $U^* = 1.41$ sheds a relative errors of 1.5%, while the maximum differences for fitted values between both trends, 2.3%, are obtained at $U^* = 3.48$. It should be remarked that the studied values of U^* are not necessarily the same for experiments and numerical simulations and therefore respective fits are used to compare results for some ranges of the reduced velocity. Similarly, the comparison between mean deflection of plates Θ (Fig. 5) provides a maximum relative error of 5.2% for Θ between fitted values at $U^* = 3.48$ (at coincident $U^* = 1.41$ the error is 3.9%). These small differences are also observable for H_r (Fig. 8a), as it is a derived magnitude from Θ. However, values of the recirculating length L_r display larger errors (see Fig. 8b), which are close to 10% for all values of U^* presented. Such discrepancies may be judged acceptable considering the simplicity of the numerical model, based on the two-dimensional assumption and the unsteady-RANS equations. In fact, this comparison of L_r provides a smaller relative error than that reported in previous study of Carini et al. (2017) for a similar D-shaped body at $Re = 32\,000$. Notwithstanding the differences, as shown therein, the U-RANS flow can be successfully used to predict major features of dominant stability mode, sensitivity and frequency at the wake.

Thus, it can be concluded that the U-RANS simulations render similar results to those obtained experimentally at a relatively low computational cost, despite the fact that that the experimental bluff body presents a finite span in the towing tank, with an aspect ratio $w/h = 7.64$. In general, the agreement between results from both approaches in term of forces and fluid–structure interaction response, can be considered good, proving the capability of simple two-dimensional turbulent numerical simulations to obtain a fair estimation of the major variables from the approximated 2D experimental problem. In this sense, Fig. 4(a) shows also that the evolution with U^* of the numerical amplitude of oscillations $\hat{\Theta}$ is very similar to the experimental trend for coincident values of U^*, which displays maximum $\hat{\Theta} < 1°$ at $U^* = 2.13$, and a very weak amplitude at larger reduced velocity. In addition, this confirms the weaker dynamic response of plates, so that the analysis of the quasi-static nature of the adaption process seems to be appropriate within the range of U^* selected here.

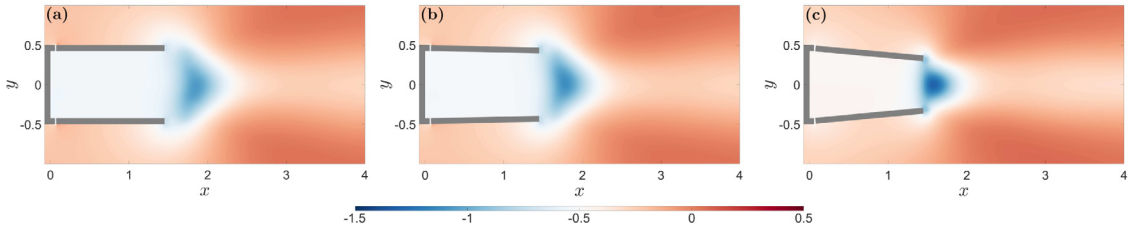

Fig. 9. Time-averaged contours of the pressure coefficient C_p and plates locations obtained from numerical simulations for $U^* = 0.01$ (a), $U^* = 1.13$ (b) and $U^* = 3.33$ (c). Respective values of the base suction coefficients are $C_b = 0.541$ (a), $C_b = 0.526$ (b) and $C_b = 0.469$ (c). C_p values range from −1.5 (blue) to 0.5 (red). (For interpretation of the references to colour in this figure legend, the reader is referred to the web version of this article.)

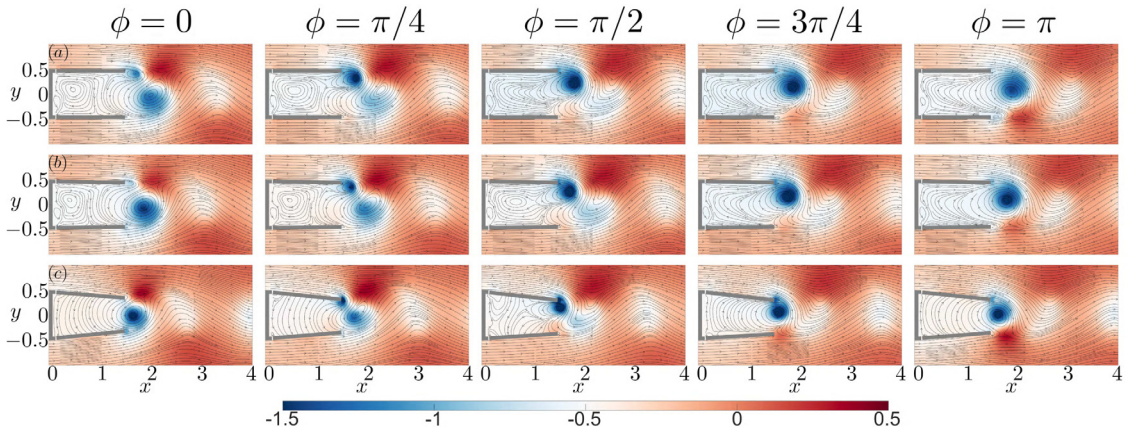

Fig. 10. Time-sequence of vortex shedding depicted by means of instantaneous snapshots of pressure coefficient c_p and corresponding flow streamlines for (a) $U^* = 0.01$, (b) $U^* = 1.13$ and (c) and $U^* = 3.33$.

On that account, numerical results may be used to study the extension of results and effect of adaption of plates beyond the range of experimental reduced velocity. As observed in Fig. 5(a), the mean deflection of plates clearly tends to an asymptotic value of 5.8°, indicating a limit on the self-adaptive process. As discussed earlier, the computation of the Vogel exponent γ (Eq. (12)), is typically used to evaluate the effective reduction of the quadratic dependence of the drag on the flow velocity. Thus, the numerical results on the drag force and its evolution with the reduced velocity U^* (Fig. 4a), allows extrapolation of the Vogel exponent towards higher values of the Cauchy number Ca (Fig. 4c) showing an increase of γ after reaching a minimum at $Ca = 52.272$. This approximation from numerical results confirms the limit on the potential decrease of the drag force beyond the range of dimensionless stiffness (either U^* or Ca) analyzed here, and justify the selection of the values for the present study.

5.2. Analysis of the wake pressure

To understand the mechanism behind the reported drag reduction induced by the plates' reorientation, the effect of such process on the near wake pressure is next discussed. In view of the good quantitative agreement reported between experimental and numerical results for values of C_x and H_r, it seems that the aerodynamic improvement is mostly governed by the mean plates' deflection Θ (see Fig. 8c and Eq. (13)), and the associated pressure modifications induced inside the cavity. To study that, the time-averaged contours of the pressure coefficient C_p and the mean deflection position of plates for selected values of the reduced velocity, $U^* = 0.01$, 1.13 and 3.33, are depicted in Fig. 9. The mean angular position of plates is also shown to illustrate the reconfiguration of the trailing edge. Additionally, the corresponding values of the time-averaged base suction coefficient, $C_b = -\langle C_{p,b} \rangle$, are also listed. First, the three selected values of U^* display the progressive displacement of plates, starting with a nearly nil mean deflection Θ for $U^* = 0.01$, that becomes $\Theta = 1.22°$ for $U^* = 1.13$ and $\Theta = 5.21°$ for $U^* = 3.33$. This process is associated with a gradual reduction of near wake bluffness and recirculating length (see trend of L_r in Fig. 8b). The reduction of the bubble size is inferred by the shrinking of the intense region of negative pressure. In particular, the local minimum becomes more negative with the reorientation of plates; however, the pressure inside the cavity recovers and becomes less negative, what consequently leads to a lower base suction coefficient (note that the base suction is positive by definition).

The reduced extension of the recirculating bubble, associated to the streamlining of the trailing part of the body induced by the plates self-adaption, affects importantly the formation length and intensity of eddies pressure. This is shown in

Fig. 10, where the sequence of vortex shedding process is depicted for the selected values of $U^* = 0.01,\ 1.13$ and 3.33, by means of instantaneous snapshots of the pressure coefficient c_p and corresponding flow streamlines along half shedding cycle. The case with $U^* = 0.01$ (Fig. 10a) can be considered as the static reference case, as there is barely no deflection of plates. Thus, the sequence displays the formation and shedding of the clockwise upper eddy, which is identified by means of streamlines and the locus of low pressure. In particular, at the beginning of the cycle, $\phi = 0$, a wide counter-clockwise eddy extends over the whole span between plates' edges, while the upper clockwise eddy starts to form. Subsequently, the upper eddy starts to widen and the pressure becomes more negative as the intensity of the eddy grows, while the lower eddy dissipates as it is convected downstream. At $\phi = 3\pi/4$, the eddy covers the whole span between plates, before being expelled into the wake, where starts to dissipate at $\phi = \pi$.

The picture is similar in Fig. 10(b,c), although the reorientation of plates reduces the extension of the eddy. It is seen that the pressure inside the eddy decreases locally, although the stronger displacement of plates prevents the eddy to enter the cavity and reduces their size. Thus, no strong recirculation of flow exists inside the cavity, as seen in Fig. 10(c). Such a dead flow-like region increases the pressure at the base, as inferred from the pressure coefficient contours and values given in Fig. 9, what ultimately translates into the important drag reductions reported in Fig. 4. In particular, the values of drag and suction coefficients computed numerically are seen to follow the relation $\Delta C_x = C_x - C_{x,ref} \simeq 1.3\Delta C_b = 1.3(C_b - C_{b,ref})$. The relation deviates slightly from the linear law of slope 1, an effect that is likely to be due to the closure of the cavity as U^* grows, as the value of C_b only considers the pressure at the base but not the effect of the pressure on the outer sides of deflected plates (Lorite-Díez et al., 2020b). In any case, the linear dependence between drag variations and base suction variations is an expected result for blunt base geometry when the pressure drag is the only source of drag.

All in all, it has been shown that the self-adaption of flexibly-hinged rigid plates induces an important base pressure recovery. Therefore, it may represent an effective solution to achieve major drag reductions in bluff vehicles, while avoiding the dynamical complexity displayed by purely flexible foils, and the disturbances that it may induce in terms of side loading and maneuverability.

6. Conclusions

The present work studies the aerodynamics of a D-shaped blunt body that implements rear flexibly-hinged rigid flaps and is subject to a turbulent flow, at $Re = 12\,000$, for different yaw angles, namely $\beta = 0°$ and $\beta = 4°$. To that aim, different flap-embedded plate properties are considered, which yield associated reduced velocities in the range $U^* = (0, 3.48]$. In particular, the effect of the system on the drag, plates displacement and near wake flow is analyzed, by means of experiments and complementary numerical simulations.

The results show that, in the range of U^* herein considered, the plates undergo an inwards quasi-static reorientation, which is symmetric for yaw angles $\beta = 0°$ and asymmetric for $\beta = 4°$. Thus, small mean deformation angles Θ are observed for values of $U^* < 1$, whereas a sharp and monotonic increase of Θ occurs for $U^* > 1$, i.e. for lower values of the hinge stiffness, with an asymptotic trend towards the larger values of U^*. Consequently, a progressive streamlining of the trailing edge is induced for both values of the incident yaw angle β, which translates into significant reductions of the associated mean drag coefficients. Such observation is especially remarkable for $U^* > 1$, with maximum values equal to 18% and 19%, obtained for the most flexible case $U^* = 3.48$, for $\beta = 0°$ and $\beta = 4°$, respectively. While computing the evolution of the Vogel exponent γ to evaluate the effect of the rear configuration on the recirculation bubble aspect ratio, it has been observed that $\gamma \simeq 0$ for low Ca number ($U^* < 1$) but displays negative values for $Ca > 3.423$ ($U^* > 1.154$). The exponent presents an experimental minimum value of $\gamma = -0.21$ at $Ca = 52.272$, the most flexible case experimentally investigated. Furthermore, numerical extrapolation of the Vogel exponent towards larger Ca values yields an increase of γ to an asymptotic value equal to -0.06, which indicates a limit on the potential reduction of the drag with the increase of flexibility. The analysis of the plates oscillations shows that, within the range of U^* selected here, the self-adaptive process can be considered quasi-static, as the amplitude of angular oscillations is very small when compared to the mean deflection of plates.

A close inspection of the near wake reveals that the inwards progressive mean displacement of the plates yields a reduction in the recirculation bubble size. The aforementioned stems from an increase of the flow momentum towards the axis in the y coordinate, which results in a narrowing of the traverse bubble height and shortening of the bubble length. A symmetric evolution of the recirculating bubble is observed for $\beta = 0°$, whereas the bubble becomes asymmetric for $\beta = 4°$, with a larger leeward clockwise vortex. The reduced extension of the recirculating bubble significantly alters the formation length and intensity of the eddies pressure. In particular, it is observed that despite the local pressure decrease in the vortices shed from the trailing edges, the plates reconfiguration reduces the eddies size and prevents them from entering the cavity, thus, creating a dead flow region with a consequent pressure increase at the body base.

In summary, the present work shows that the use of low dynamical order, adaptive control systems to reduce the drag of a bluff body and manipulate the wake behind it might constitute an effective alternative to more complex, purely flexible solutions. These solutions are more robust and easier to implement than purely flexible systems, and yield comparable reductions in aerodynamic drag, while circumvent the complex solid dynamics and associated disturbances observed in flexible foils, which renders the former more appealing for engineering applications. In particular, the device herein studied, which consists of flexibly-hinged rigid plates, has been shown to induce significant drag reductions based on trailing edge reconfiguration. These kinds of systems might be of use for both land heavy transport, with air as the

working fluid, or ocean applications, with water as the working fluid. On this matter, it is important to highlight that the effect of the density and associated added mass may alter the dynamic response of the flaps, especially in terms of maximum amplitude, which may have direct impact on the maneuverability of vehicle. Additionally, the higher flow velocity in air required to achieve the same Reynolds number defined here, implies that the stiffness of the hinge junction may necessarily rise to increase the natural frequency of the system, and consequently, to keep the reduced velocity within the range of interest ($U^* < 5$) also in air. Hence, some intermediate steps and a thorough study under more realistic conditions (e.g. three-dimensional wake, cross-flow) would be required prior to any applied system is designed and tested in air.

CRediT authorship contribution statement

C. García-Baena: Investigation, Validation, Formal analysis, Software, Writing. **J.M. Camacho-Sánchez:** Investigation, Validation, Formal analysis, Writing. **M. Lorite-Díez:** Investigation, Validation, Visualization, Writing. **C. Gutiérrez-Montes:** Software, Methodology, Supervision, Writing, Resources. **J.I. Jiménez-González:** Conceptualization, Methodology, Investigation, Formal analysis, Writing, Supervision, Resources, Project administration, Funding acquisition.

Declaration of competing interest

The authors declare that they have no known competing financial interests or personal relationships that could have appeared to influence the work reported in this paper.

Data availability

Data will be made available on request.

Acknowledgments

This work is a result of Project FEDER-UJA 1262764, funded by the Junta de Andalucía, Universidad de Jaén and European Union; and Project PDC2021-121288-I00, financed by the Spanish MCIN/ AEI/10.13039/501100011033/ and the European Union NextGenerationEU/PRTR. M.L.D also acknowledges the support from FJC2020-043093-I grant by the Spanish AEI. The authors are also grateful to Prof. C. Martínez-Bazán for fruitful discussions and the critical reading of the manuscript.

References

Abdi, R., Rezazadeh, N., Abdi, M., 2019. Investigation of passive oscillations of flexible splitter plates attached to a circular cylinder. J. Fluids Struct. 84, 302–317.
Alben, S., Shelley, M., Zhang, J., 2002. Drag reduction through self-similar bending of a flexible body. Nature 420, 479–481.
Assi, G., Bearman, P., Kitney, N., 2009. Low drag solutions for suppressing vortex-induced vibration of circular cylinders. J. Fluids Struct. 25 (4), 666–675.
Bonnavion, G., Cadot, O., 2019. Boat-tail effects on the global wake dynamics of a flat-backed body with rectangular section. J. Fluids Struct. 89, 61–71.
Carini, M., Airiau, C., Debien, A., Léon, O., Pralits, J.O., 2017. Global stability and control of the confined turbulent flow past a thick flat plate. Phys. Fluids 29 (2), 024102.
Choi, H., Jeon, W.-P., Kim, J., 2008. Control of flow over a bluff body. Annu. Rev. Fluid Mech. 40 (1), 113–139.
Choi, H., Lee, J., Park, H., 2014. Aerodynamics of heavy vehicles. Annu. Rev. Fluid Mech. 46 (1), 441–468.
Darbandi, M., Fouladi, N., 2016. Numerical study of flow-induced oscillations of two rigid plates elastically hinged at the two ends of a stationary plate in a cross-flow. J. Fluids Struct. 66, 147–169.
Deb, D., Shetty, P., Poddar, K., Kumar, S., 2020. Flow induced oscillation of two rigid rectangular plates in a side-by-side configuration. J. Fluids Struct. 99, 103133.
García-Baena, C., Jiménez-González, J.I., Gutiíerrez-Montes, C., Martínez-Bazán, C., 2021b. Numerical analysis of the flow-induced vibrations in the laminar wake behind a blunt body with rear flexible cavities. J. Fluids Struct. 100, 103194.
García-Baena, C., Jiménez-González, J.I., Martínez-Bazán, C., 2021a. Drag reduction of a blunt body through reconfiguration of rear flexible plates. Phys. Fluids 33 (4), 045102.
Gosselin, F., De Langre, E., Machado-Almeida, B.A., 2010. Drag reduction of flexible plates by reconfiguration. J. Fluid Mech. 650, 319–341.
Harder, D.L., Speck, O., Hurd, C.L., Speck, T., 2004. Reconfiguration as a prerequisite for survival in highly unstable flow-dominated habitats. J. Plant Growth Regul. 23 (2), 98–107.
Hucho, W.-h., Sovran, G., 1993. Aerodynamics of road vehicles. Annu. Rev. Fluid Mech. 25 (1), 485–537.
International Energy Agency Report, 2018. Emissions from Fuel Combustion.
Jasak, H., Tukovic, Z., 2007. Automatic mesh motion for unstructured finite volume method. Trans. FAMENA 30, 1–18.
Jasak, H., Tukovic, Z., 2010. Dynamic mesh handling in OpenFOAM applied to fluid-structure interaction simulation. In: V European Conference on Computational Fluid Dynamics, ECCOMAS CFD 2010.
Jiménez-González, J.I., 2013. Study of the Stability of Jets and Wakes. Application to the Wake Past Slender Bodies with Blunt Trailing Edge (Ph.D. thesis). Universidad de Jaén.
Jiménez-González, J.I., García-Baena, C., Aceituno, J., Martínez-Bazán, C., 2021. Flow-induced vibrations of a hinged cavity at the rear of a blunt-based body subject to laminar flow. J. Sound Vib. 495, 115899.

Khalighi, B., Zhang, S., Koromilas, C., Balkanyi, S., Bernal, L.P., Iaccarino, G., Moin, P., 2001. Experimental and computational study of unsteady wake flow behind a bluff body with a drag reduction device. SAE Trans. 110 (6), 1209–1222.
Lorite-Díez, M., Jiménez-González, J.I., Gutiérrez-Montes, C., Martínez-Bazán, C., 2017. Drag reduction of slender blunt-based bodies using optimized rear cavities. J. Fluids Struct. 74, 158–177.
Lorite-Díez, M., Jiménez-González, J.I., Gutiérrez-Montes, C., Martínez-Bazán, C., 2018. Effects of rear cavities on the wake behind an accelerating D-shaped bluff body. Phys. Fluids 30 (4), 044103.
Lorite-Díez, M., Jiménez-González, J.I., Pastur, L., Cadot, O., Martínez-Bazán, C., 2020b. Drag reduction on a three-dimensional blunt body with different rear cavities under cross-wind conditions. J. Wind Eng. Ind. Aerodyn. 200, 104145.
Lorite-Díez, M., Jiménez-González, J.I., Pastur, L., Martínez-Bazán, C., Cadot, O., 2020a. Experimental analysis of the effect of local base blowing on three-dimensional wake modes. 883, A53,
Lu, L., Guo, X.-l., Tang, G.-q., Liu, M.-m., Chen, C.-q., Xie, Z.-h., 2016. Numerical investigation of flow-induced rotary oscillation of circular cylinder with rigid splitter plate. Phys. Fluids 28 (9), 093604.
Martín-Alcántara, A., Sanmiguel-Rojas, E., Gutiérrez-Montes, C., Martínez-Bazán, C., 2014. Drag reduction induced by the addition of a multi-cavity at the base of a bluff body. J. Fluids Struct. 48, 347–361.
Mazellier, N., Feuvrier, A., Kourta, A., 2012. Biomimetic bluff body drag reduction by self-adaptive porous flaps. C. R. Méc. 340 (1), 81–94.
Menter, F.R., 1994. Two-equation eddy-viscosity turbulence models for engineering applications. AIAA J. 32 (8), 1598–1605.
NASA Langley Research Center, Rumsey, C., 2015. Menter Shear Stress Transport Model. Langley Research Center.
OpenCFD, 2016. OpenFOAM User Guide Version 4.0. OpenFOAM Foundation.
Park, H., Lee, D., Jeon, W.-P., Hahn, S., Kim, J., Kim, J., Choi, J., Choi, H., 2006. Drag reduction in flow over a two-dimensional bluff body with a blunt trailing edge using a new passive device. J. Fluid Mech. 563, 389–414.
Pastoor, M., Henning, L., Noack, B.R., Kind, R., Tadmor, G., 2008. Feedback shear layer control for bluff body drag reduction. J. Fluid Mech. 608, 161–196.
Peng, J., Wang, T., Yang, T., Sun, X., Li, G., 2018. Research on the aerodynamic characteristics of tractor-trailers with a parametric cab design. Appl. Sci. (Switzerland) 8.
Sanmiguel-Rojas, E., Jiménez-González, J.I., Bohorquez, P., Pawlak, G., Martínez-Bazán, C., 2011. Effect of base cavities on the stability of the wake behind slender blunt-based axisymmetric bodies. Phys. Fluids 23 (11), 114103.
Satheesh, S., Huera-Huarte, F.J., 2019. Effect of free surface on a flat plate translating normal to the flow. Ocean Eng. 171, 458–468.
Szodrai, F., 2020. Quantitative analysis of drag reduction methods for blunt shaped automobiles. Appl. Sci. 10, 4313.
Thielicke, W., Stamhuis, E., 2014. PIVlab towards user friendly, affordable and accurate digital particle image velocimetry in MATLAB. J. Open Res. Softw. 2 (1), e30.
Verzicco, R., Fatica, M., Iaccarino, G., Moin, P., Khalighi, B., 2002. Large eddy simulation of a road vehicle with drag-reduction devices. AIAA J. 40 (12), 2447–2455.
Vogel, S., 1989. Drag and reconfiguration of broad leaves in high winds. J. Exp. Bot. 40 (8), 941–948.
Wood, R.M., 2006. A discussion of a heavy truck advanced aerodynamic trailer system. SOLUS-Solut. Technol..
Wu, J., Shu, C., Zhao, N., 2014. Numerical investigation of vortex-induced vibration of a circular cylinder with a hinged flat plate. Phys. Fluids 26 (6), 063601.
Zhang, X., Nepf, H., 2020. Flow-induced reconfiguration of aquatic plants, including the impact of leaf sheltering. Limnol. Oceanogr. 65 (11), 2697–2712.